From Glacier Facies to SAR Backscatter Zones via GPR

Kirsty Langley, Svein-Erik Hamran, Kjell Arild Høgda, Rune Storvold, *Member, IEEE*, Ola Brandt, Jack Kohler, and Jon Ove Hagen

***Abstract*—We present a comparison between data acquired with frequency-modulated ground-penetrating radar (GPR) and satellite synthetic aperture radar (SAR). Both radars are polarimetric and operate at a center frequency of 5.3 GHz. The field site is the polythermal glacier Kongsvegen, Svalbard. Along glacier GPR profiles cover the ablation area and the accumulation area, where the latter consists of superimposed ice (SI) and firn. The glacier facies are clearly identifiable on the GPR profiles, although we show that the copolarized response is better for distinguishing different ice zones, whereas the SI–firn boundary is most obvious in the cross-polarized response. A calibrated backscatter coefficient is calculated for the GPR data and compared with the SAR backscatter coefficient. The SAR zones are in very good agreement with the GPR-derived glacier facies. We show that, in the ablation area, the SAR response is dominated by backscatter from the previous summer surface. In the SI and firn areas, it is dominated by sources below the previous summer surface.**

***Index Terms*—Backscatter, glacier facies, ground-penetrating radar (GPR), synthetic aperture radar (SAR).**

I. Introduction

SATELLITE remote sensing is widely perceived as an invaluable tool for monitoring and assessing the past and current state of the world's glaciers [1], [2]. Synthetic aperture radar (SAR) is particularly valuable in polar regions because it operates independently of daylight and is unaffected by weather (although weather strongly affects the properties that SAR measures). This has allowed less accessible glaciers to be monitored throughout their annual mass balance cycle [3]–[5]. To facilitate the study of glaciers from space, a number of classification systems have been suggested to identify the different zones on the glacier mapped by SAR [6], [7] (and references therein). Making the connection between SAR zones and glacier facies is considered to be somewhat problematic because the SAR glacier zones are dynamic on time scales of days to weeks, whereas glacier facies are based upon properties integrated over periods of years [3].

Snow cover plays an important role in temporal studies because, when just a small amount of liquid water is present, the backscatter properties change significantly [8], [9]. However, in early spring, the snowpack is mostly dry, and the underlying glacier (to depths of several meters) influences the backscatter [10]–[14]. Thus, at this time, the SAR signal incorporates the longer time-scale signal that defines glacier facies.

Ground-penetrating radar (GPR) is used extensively to map glacier facies [15]–[19] and is applicable in the context of SAR interpretation because it provides information on both the short- and long-term buildup of the glacier. Langley *et al.* [14] demonstrated that a 5.3-GHz GPR could be used to couple the backscatter contribution from different glacial facies to 5.3-GHz SAR zones. This paper expands on this work by coupling polarimetric GPR and SAR data.

We present a grid of polarimetric 5.3-GHz GPR profiles along the length of Kongsvegen, a high-Arctic polythermal glacier. The GPR profiles clearly map the different glacier facies and show directly how the polarimetric 5.3-GHz backscatter intensities respond to different glacier facies. Because our GPR operates at the same frequency as the Envisat satellite SAR instrument, we are able to investigate the link between glacier facies and SAR zones.

II. Field Site: Kongsvegen, Svalbard

The data that we present focus on the 26-km-long glacier Kongsvegen, which is situated at approximately 79° N on the northwest of the Spitsbergen archipelago (inset of Fig. 1). Kongsvegen covers an area of approximately 100 km^2, draining north westward from an elevation of 800 m a.s.l. to sea level. It has a gentle surface slope of 0.5°–2°, which reduces slope-induced effects in the SAR images. This is a polythermal glacier that is frozen to the bed at the snout and along the mountain sides [20]. The accumulation area is temperate, and a temperate basal layer extends into the ablation area [18]. The accumulation area is split into two zones: a superimposed ice (SI) area and a firn area. The firn area corresponds to the wet-snow and percolation zones discussed in [7]. There is no dry-snow zone on Kongsvegen. The equilibrium line lies at approximately 500 m a.s.l. The mass balance is approximately zero [21],

Manuscript received November 19, 2007. This work was supported in part by the Norwegian Research Council (NFR) under Contract 155834 and in part by the Norwegian Polar Institute under an Arctic research grant.

K. Langley was with the University of Oslo, 0317 Oslo, Norway. She is now with the Norwegian Polar Institute, 9296 Tromsø, Norway, and also with the Institute of Physics and Technology, University of Tromsø, 9037 Tromsø, Norway (e-mail: kirsty.langley@npolar.no).

S.-E. Hamran and J. O. Hagen are with the University of Oslo, 0317 Oslo, Norway (e-mail: Svein-Erik.Hamran@ffi.no; j.o.m.hagen@geo.uio.no).

K. A. Høgda and R. Storvold are with the NORUT Information Technology, 9294 Tromsø, Norway (e-mail: kjell.arild.hogda@itek.norut.no; Rune.Storvold@itek.norut.no).

O. Brandt and J. Kohler are with the Norwegian Polar Institute, 9296 Tromsø, Norway (e-mail: ola.brandt@npolar.no; jack.kohler@npolar.no).

Color versions of one or more of the figures in this paper are available online at http://ieeexplore.ieee.org.

Digital Object Identifier 10.1109/TGRS.2008.918648

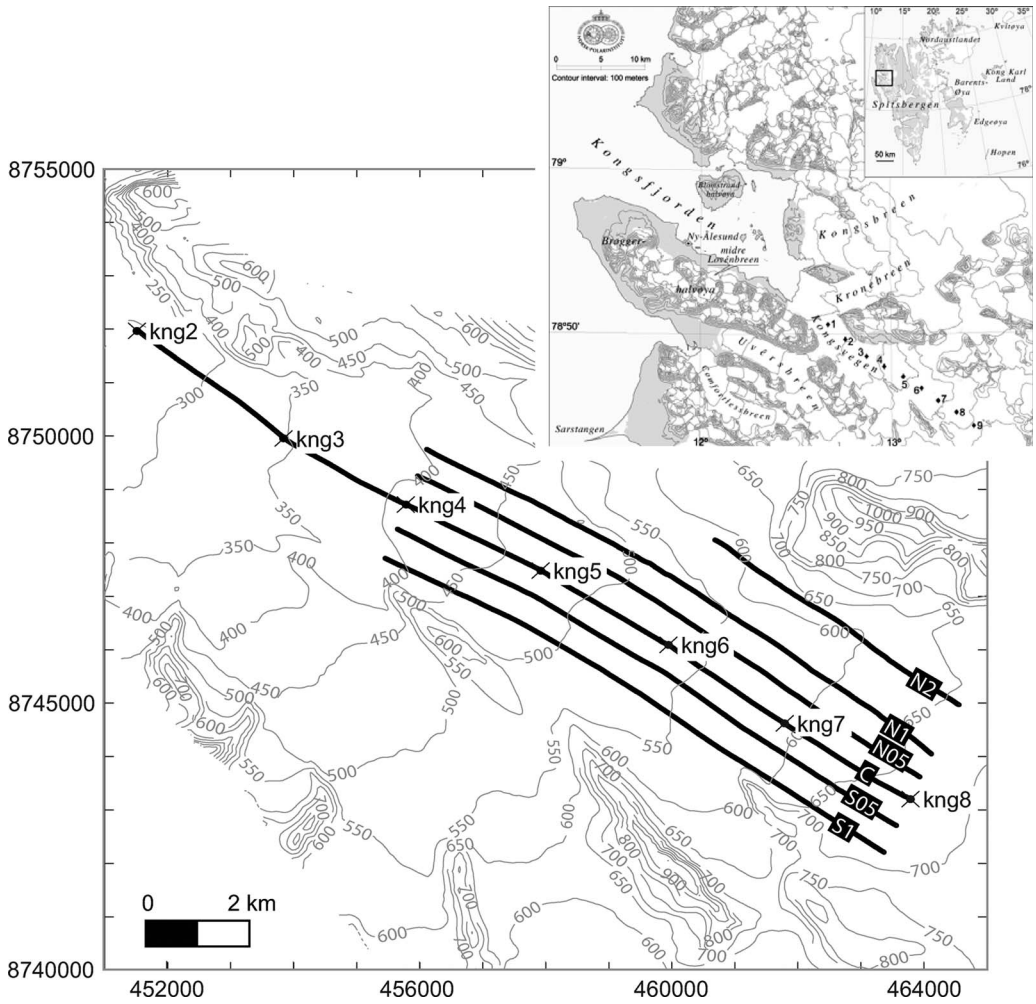

Fig. 1. Field site Kongsvegen (shown on a UTM grid projection) located on the northwest of Spitsbergen (inset). Points numbered 1–9 along the glacier center line are the mass balance stakes, which are used here as marker points in our GPR surveys. The GPR lines (shown in black) run along and parallel to the center line of the glacier. Profiles S1 and N2 are shown in Figs. 6 and 7, respectively.

although, in the last seven years, negative balance years have dominated [22].

This is a surge-type glacier. The last surge (which occurred in 1948 [20]) is thought to be the cause of a discrete boundary between SI and underlying glacier ice (GI), as mapped by GPR [23]. This surge event is also believed to have formed the characteristic herringbone-like structure within the GI, as seen by GPR, in the upper parts of the ablation area. This structured ice extends upglacier beneath the SI. We shall refer to ice showing this structure as herringbone ice (HBI). Ice in the ablation area not showing this structure will be referred to as GI. HBI has a different backscatter signature to GI and SI but is similar enough that it complicates interpretation of the ice facies for both the GPR and SAR.

The mean annual air temperature in Ny Ålesund (the nearest settlement) is $-6.3\,^{\circ}$C (42 m a.s.l., 1961–1990) (www.met.no). However, due to the maritime climate, temperatures can fluctuate above $0\,^{\circ}$C, with rain and melt events occurring all year round on the glacier. Such events alter the density composition of the snow and firn packs through refreezing of percolating meltwater at depth to form ice lenses and pipes. It is the density contrast and roughness caused by these inhomogeneities that cause significant backscatter at 5.3-GHz frequencies [11].

III. GPR Data and Processing

The radar used to acquire the 5.3-GHz data is a fully polarimetric frequency-modulated continuous-wave radar. The data acquisition sequence is such that, first, one polarization is transmitted and both are received, then the other is transmitted and both are received, thereby recovering the full polarization matrix. Details of this system are given in [24].

The antennas are dual-polarized quad-ridged horns with a gain of 6.6–7.4 dB and a 3-dB beamwidth of 70°–65° in both the X and Y planes over the bandwidth used. The X-axis is defined as the direction of travel of the radar (i.e., along profile). The antennas are suspended some 30 cm above the snow surface to the side of a snow scooter sledge (Fig. 2). This puts the surface in the far field. The system sweeps from 4.8 to 5.8 GHz, giving it a center frequency of 5.3 GHz and a wavelength of 5.6 cm in air. The bandwidth of 1 GHz should yield a resolution of 0.15 cm in air [25], but with the Hamming window (applied to reduce the sidelobes), this is increased to 19 cm in air or 10 cm in ice ($\varepsilon_r = 3.15$). The data are converted to the time domain with a fast Fourier transform algorithm. The time step within each trace is 0.14 ns.

Traces were obtained approximately every 0.5 m along the profile. This should not be confused with the distance traveled

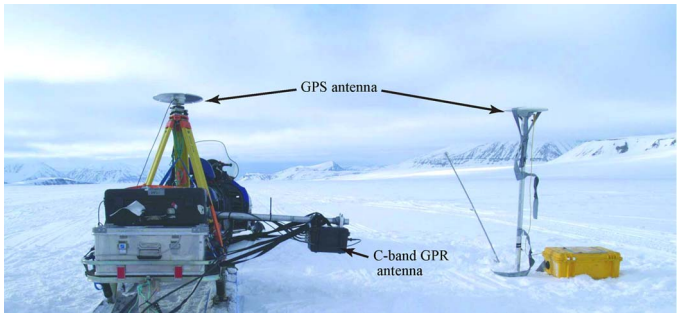

Fig. 2. Field setup of the 5.3-GHz GPR and GPS antennas.

during the frequency sweep, which takes just 20 ms, or 0.04 m at a driving speed of 8 km · h^{-1}. We are aware that the footprint therefore changes within a single sweep, but we believe that, because we are looking at larger scale structures, this is of little consequence.

The GPR is calibrated using a technique proposed by Sarabandi *et al.* [26] for field calibration of polarimetric radars. The method determines the deviation in the antenna phase and amplitude from the nominal gain values. These field transfer functions are obtained using two reference targets: a sphere and a second target with a strong cross-polarized radar cross section (such as a diplane). This calibration method is particularly applicable to field operations, as it does not require accurate alignment of the calibration targets or knowledge of the radar cross section of the depolarizing target.

The scattering amplitudes S_{mn}'s (where m and n denote the polarization (X or Y) of the scattered and incident fields, respectively) are related to the radar cross section σ_{mn} of the target by

$$\sigma_{mn} = 4\pi |S_{mn}|^2. \tag{1}$$

The voltage received at the antenna by illumination of a target at distance r can be expressed as

$$E_{mn} = \frac{K}{r^2} e^{-i2kr} R_m T_n S_{mn} \tag{2}$$

where

$$K = \left[\frac{P_t G_t G_r \lambda^2}{(4\pi)^2} \right]^{1/2} \tag{3}$$

with P_t being the power transmitted and G_t and G_r being the nominal gains of the transmit and receive antennas, respectively. The field transfer functions for the antennas are represented by the quantities R_m and T_n. The components of the scattering matrix are calibrated using the following [26]:

$$S^u_{XX} = \left(\frac{E^u_{XX}}{E^0_{XX}} \right) \left(\frac{r_u}{r_0} \right)^2 e^{-2k(r_0 - r_u)} S_0 \tag{4}$$

$$S^u_{YY} = \left(\frac{E^u_{YY}}{E^0_{YY}} \right) \left(\frac{r_u}{r_0} \right)^2 e^{-2k(r_0 - r_u)} S_0 \tag{5}$$

$$S^u_{YX} = \left(\frac{E^u_{YX}}{\sqrt{K_1 K_2}} \right) \left(\frac{r_u}{r_0} \right)^2 e^{-2k(r_0 - r_u)} S_0 \tag{6}$$

$$S^u_{XY} = \sqrt{\frac{K_1}{K_2}} E^u_{XY} \left(\frac{r_u}{r_0} \right)^2 e^{-2k(r_0 - r_u)} S_0 \tag{7}$$

where the subscript and superscript "0" denotes quantities associated with the metal sphere and "u" denotes quantities associated with a target with unknown scattering matrix (in this case, our field measurements). The quantities K_1 and K_2 are defined as

$$K_1 = \frac{E^C_{YX}}{E^C_{XY}}$$
$$K_2 = E^0_{XX} E^0_{YY} \tag{8}$$

where the superscript "C" denotes the cross-polarization target. Combining (4)–(7) with (1) gives the calibrated radar cross section for each polarization. All four components of the scattering matrix can then be calibrated.

We use a sphere with radar cross section 0.1 m^2 and a diplane as our calibration targets. These were placed at a distance of 1 m from the antennas. The first Fresnel zone at 1 m is 0.47 m. To improve the signal-to-noise ratio, the calibration measurements were performed both with and without the targets to remove the background signature from the surroundings. The calibrated cross sections are divided by the illuminated volume (where the radiation pattern is based on a 3-dB beamwidth of 64°) to give a scattering cross section per unit volume.

In order to incorporate ray bending and velocity effects due to permittivity changes, the range and volume terms are based on velocity profiles from common midpoint (CMP) measurements and snow density measurements [27]. The CMP measurements were made in 2004 at stakes 6, 7, and 8. The velocity is interpolated between these points. The firn cores were retrieved in 2005 from approximately 50 m upglacier of stake 8. The snow density measurements were made in 2005 at each of the stakes.

Our intention is to compare the GPR data with the SAR data. SAR measures the backscatter coefficient for a particular resolution cell. This is the integrated contribution from all targets within the time window to the depth of penetration. To achieve a comparable variable from the GPR data, we integrate the scattering cross sections incoherently for each trace from 0 ns to the depth equivalent of 100 ns [14]. The calibrated backscatter coefficient σ° at each trace location is thus

$$\sigma^0 = \int_0^r \sigma_{mn} dr. \tag{9}$$

It should be noted that loss due to attenuation is not compensated for. Thus, the calibrated scattering cross section includes the measured loss, and the backscatter coefficient calculated with (9) is therefore weighted by the loss.

Six profiles oriented parallel to the center line were obtained on Kongsvegen with the GPR in spring 2005 (Fig. 1). DGPS was used to determine the position of the profiles to an horizontal accuracy of approximately 0.1 m. Positioning of individual traces along the profiles was determined by both the recorded GPR time and by even distribution of the traces between known stop points. Thus, the accuracy of the trace location is somewhat less than that of the DGPS.

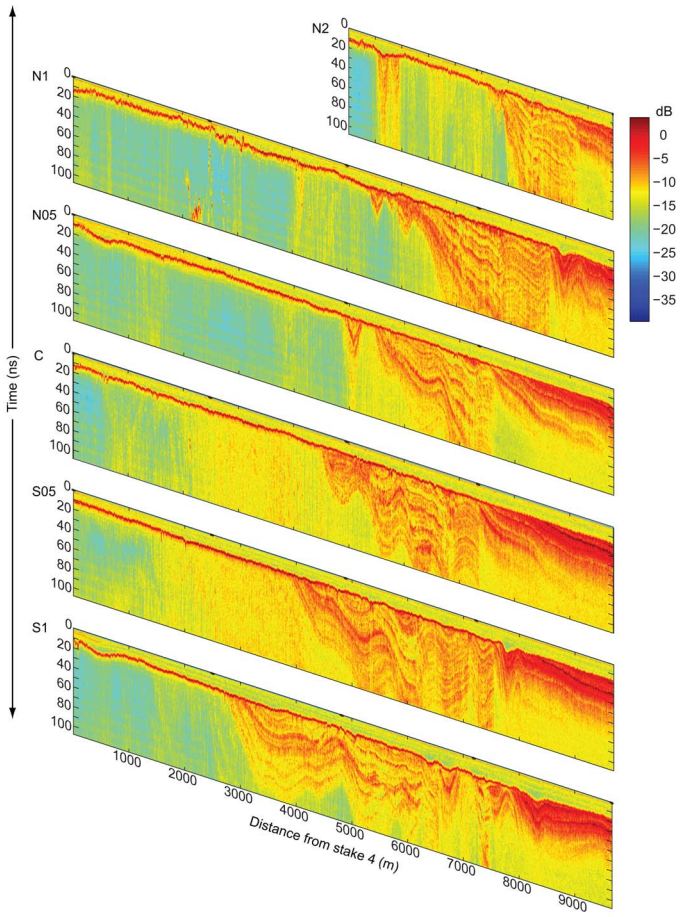

Fig. 3. Copolarized 5.3-GHz GPR profiles (location shown in Fig. 1).

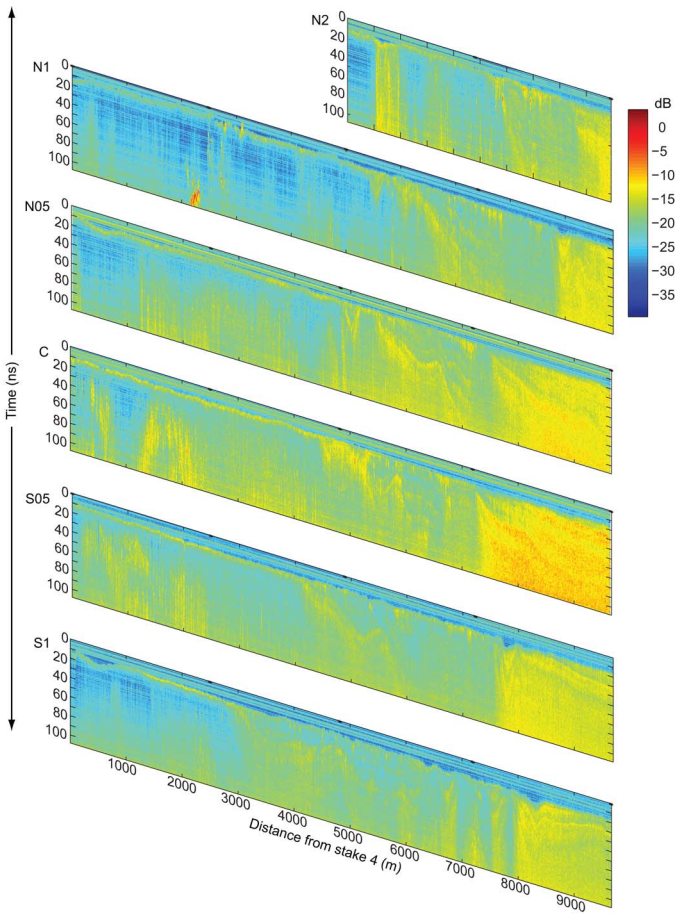

Fig. 4. Cross-polarized 5.3-GHz GPR profiles (location shown in Fig. 1).

The YY- and YX-polarized data are presented here as representation of the co-and cross-polarized responses, respectively (hereafter referred to as co- and cross-pol). Both X and Y planes lie in the plane parallel to the glacier surface. The X plane lies in the direction of the GPR movement (i.e., along glacier), and the Y plane is perpendicular to the X plane (i.e., in the across-glacier direction).

The GPR profiles are presented in two ways: 1) as image scans, indicating how the calibrated scattering cross section varies in two dimensions over distance (along glacier) and two-way travel time. The calibrated profiles used in our interpretation are shown in Figs. 3 and 4. Data in these plots have been filtered with a 10-m running mean and downsampled to 5-m intervals to reduce display aliasing; 2) as line plots to show the integrated backscatter coefficient along the profiles. A running mean of 30 m (the horizontal resolution of the SAR images) has been applied to these data, followed by downsampling to 10-m intervals. To account for the difference in look angle between the GPR and SAR, a static correction of -20 dB has been applied to the GPR backscatter coefficients [28]. This is discussed further in Section VI.

IV. SAR Data and Processing

SAR scenes from the ASAR instrument onboard the Envisat satellite are used in this paper. All scenes were acquired in alternating polarization mode and ascending orbit. In this phase of the orbit, the satellite flight path is approximately parallel to the glacier center line, and the radar look direction is across glacier (toward northeast).

The scenes were processed according to [29] and [30] to produce geocoded calibrated backscatter images. No corner reflectors were used to geolocate the SAR images. Instead, we performed a careful geocoding and calibration of the scene using a high-resolution digital elevation model and cross correlation with a reference image which has been adjusted using tie points and coast line. This gives a relative coregistration accuracy that is better than 0.2 pixels and a subpixel absolute accuracy [29], [30]. The processing results in images with a resolution of 30 m in both range and azimuth.

Ideally, we would like to compare the most vertical-looking SAR scenes with our nadir-looking GPR, but because there are so few scenes at IS1 (15.0°–22.9°) for the period that we consider, we combine both IS1 and IS2 (19.2°–26.7°) scenes. Close inspection of the extracted backscatter profiles shows that there is approximately 1–2-dB difference between the two look angles, which is probably caused by the higher magnitude of the surface reflection for the IS1 look angle [Fig. 5(a)]. The shape of the backscatter response over the profile distance is very similar.

In addition, because we have so few scenes, both HH and VV polarizations are combined to form the co-pol image, and

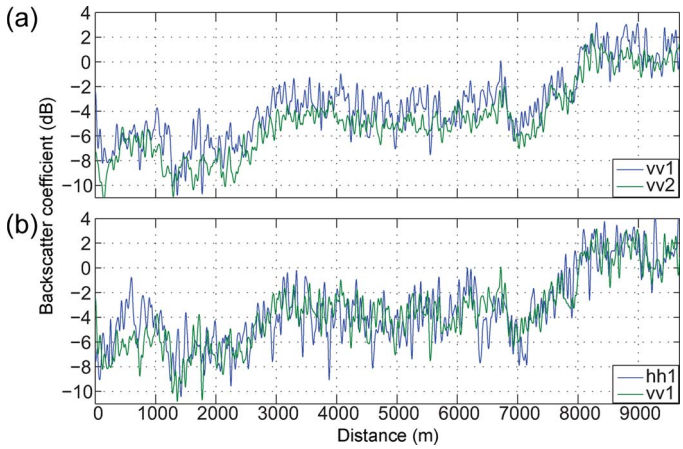

Fig. 5. SAR backscatter coefficient along profile S1. (a) IS1 and IS2 look angles at VV polarization. (b) IS1 look angle for HH and VV polarizations.

TABLE I
SAR SCENES COMBINED TO PRODUCE THE CO- AND CROSS-POLARIZED SAR DATA PRESENTED HERE

Polarisation	ASAR scenes
Co	IS1 HH 23/04/2005
	IS1 VV 26/04/2005
	IS1 VV 29/04/2005
	IS2 VV 02/02/2005
	IS2 VV 09/03/2005
	IS2 VV 13/04/2005
	IS2 VV 16/04/2005
	IS2 VV 02/05/2005
	IS2 VV 18/05/2005
Cross	IS1 HV 23/04/2005
	IS1 VH 26/04/2005
	IS1 VH 29/04/2005
	IS2 VH 02/02/2005
	IS2 VH 09/03/2005
	IS2 VH 13/04/2005
	IS2 VH 16/04/2005
	IS2 VH 02/05/2005
	IS2 VH 18/05/2005

all HV and VH acquisitions form the cross-pol image (Table I). There are some localized differences between the HH and VV polarizations and, most notably, in the ice facies areas where the reflection from the surface is more important [Fig. 5(b)].

In spite of the minor differences noted previously, combining the polarizations is justified because the SAR polarization planes are not anyway equivalent to the GPR polarization planes. The SAR H plane lies parallel to the glacier surface, as do both the X and Y planes of the GPR. There is no GPR equivalent of the SAR V plane. H-polarized SAR scenes would therefore give the most realistic comparison of the two systems. However, because we only have one HH-polarized scene (Table I), we have decided to combine all. Averaging in this way, we smooth the profile by reducing speckle.

V. RESULTS

A. Glacier Facies as Represented by 5.3-GHz GPR

The focus of the GPR profiles was the central upper part of the glacier from stake 4 to stake 8 (Fig. 1). The profiles pass through three different glacier facies including GI, SI, and firn (Fig. 6). Just to recap from Section II: the ice facies in the ablation area can be subdivided into two GPR zones, which are termed here as GI and HBI. These zones are both in the ablation area but are two distinct radar zones. Each of the four zones, GI, HBI, SI and firn, have a distinct GPR backscatter signature caused by the different media structure and composition. These characteristics are described hereafter.

The profiles were acquired in spring, so the uppermost layer seen in the GPR profiles (from 0 to approximately 15 ns) is the winter snowpack [Fig. 6(a)]. The previous year's summer surface, PSS (i.e., the interface at the base of the winter snowpack between new winter snow and the surface exposed at the end of the previous summer), is clearly visible in both the co- and cross-pol responses. The magnitude of the incoherent scattering component at this interface is variable within the ice facies, as indicated by the cross-pol response. Sometimes, it is greatest in the HBI area (1400–2500 m in profile S1 [Fig. 6(b)] and sometimes in the SI area (500–1000 m [Fig. 7(b)]). The incoherent response from this interface is weaker in the firn area than in the ice facies downglacier.

The GI area is the area of lowest backscatter for both co- and cross-pols due to the lack of internal scattering sources. The major source of backscatter here is the PSS, although on occasions when deeper scattering sources are observed, for example, 800–1000 m in profile S1 [Fig. 6(b)].

The HBI has, in general, higher backscatter than the GI at both polarizations. The HBI zone is distinguished from the SI in the co-pol response by the lower intensity returns and general lack of horizontal structure. The cross-pol signature in the HBI is more complicated. The main incoherent scattering centers seem to be negatively correlated to the areas of greatest co-pol response, for example, 1500–2500 m in Fig. 6(b). In addition, these scattering sources tend to be disconnected from the PSS. Negatively correlated coherent and incoherent scattering areas are also seen in the complex SI area in profile S1 [Fig. 6(a) and (b), 6500–8000 m].

Within the SI, permittivity differences most likely arise due to variations in the air bubble size and distribution [27]. This varies most significantly vertically through the ice column, hence the layering, and is related to the conditions under which a particular layer was formed [31], [32]. We suggest permittivity contrasts between layers with differing fractional volumes of bubbles create approximately smooth interfaces at which coherent reflections occur. The relatively high magnitude of the coherent reflections allows individual layers to be depicted well with the co-pol [Fig. 6(a)]. Imperfections at the boundary between two layers created, for example, by the air-bubble size and distribution, result in incoherent scattering. Volume scattering from the ice volume between the interfaces occurs to a lesser extent and is also attributed to the size and distribution of the air bubbles.

The firn area contains both thin ice lenses and ice layers with thicknesses up to several tens of centimeters. The thin lenses (< 5 cm thick) have a limited spatial extent, whereas the thicker layers are continuous for several kilometers. We have also observed numerous vertical ice fingers in firn cores (not described here). Coherent scattering occurs at the firn/ice interfaces (because this is a nadir-looking radar) and dominates the co-pol

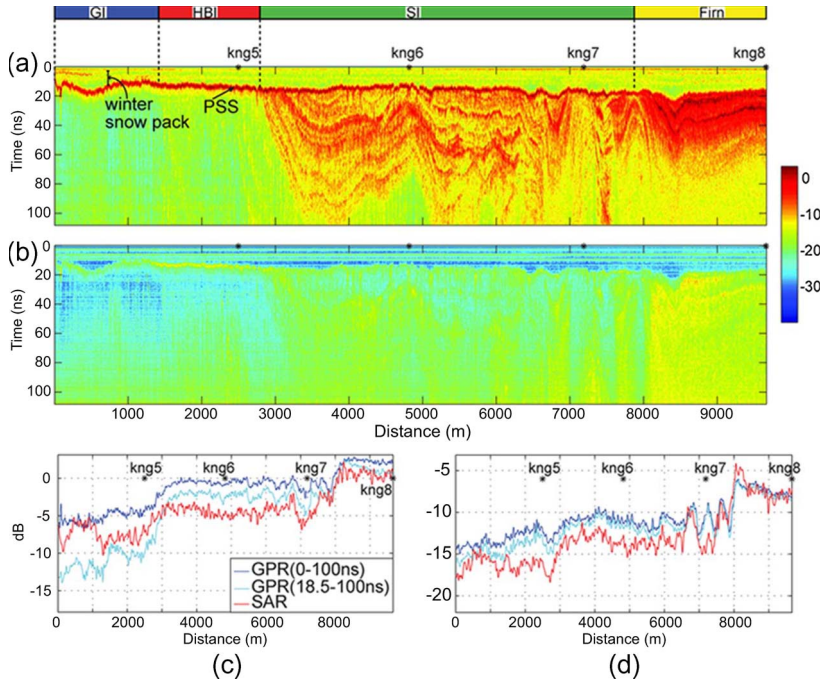

Fig. 6. Profile S1 (location shown in Fig. 1). (a) GPR copolarized radar cross section. (b) GPR cross-polarized radar cross section. The different glacier zones are labeled in the color bar at the top. Blue = glacier ice, red = herringbone ice, green = superimposed ice, and yellow = firn. kng5–kng8 correspond to the stake numbers shown in Fig. 1. The lower panels give the GPR and SAR backscatter coefficient for (c) copolarized and (d) cross-polarized.

response in the first 60 ns. Below this, incoherent scattering dominates. The cross-pol response shows that depolarized scattering occurs throughout the firn column [Fig. 6(b)] and is very much more effective in the firn area than in the ice facies downglacier. Langley *et al.* [27] suggest that most scattering is caused by the many smaller ice lenses and fingers, whereas scattering from within the thicker ice layers is relatively low.

While the different glacier facies are fairly easy to distinguish using the co- and cross-pol scattering cross sections (Figs. 3 and 4), the backscatter coefficient [the integrated radar cross section (9)] does not allow for such an easy interpretation of the glacier facies [Fig. 6(c) and (d)]. This parameter sheds light on some of the difficulties that may arise in interpreting glacier facies from SAR zones.

The co-pol backscatter coefficient increases upglacier from GI to HBI to SI [Figs. 6(c) and 7(c)]. Sometimes, a further increase occurs in the firn, but often, the SI and firn cannot be distinguished on the GPR co-pol backscatter coefficient alone (Fig. 7(c), 3000–4900 m). This is despite the fact that the radar cross section over depth is very distinct for the two facies (Fig. 7(a), 3000–4900 m). At cross-pol, the ice facies are somewhat less consistent in nature. This is particularly so in the GI and HBI areas where high-backscatter areas of similar magnitude and extent can occur in both areas. The transition from the ice to the firn facies is nearly always clear because depolarization of the electromagnetic wave is much more efficient in the firn than in the ice facies.

The conclusion therefore is that the co-pol configuration is best for distinguishing the different ice facies and that the cross-pol configuration is best suited for delimiting the SI–firn boundary.

The nadir-looking geometry of the GPR means that the PSS gives a high coherent backscatter contribution compared to what we would expect the side-looking SAR to receive from this interface. This will effectively mask subtle contributions at depth in the co-pol GPR signature. Removing the contribution of this interface from the GPR backscatter coefficient (i.e., allowing the integration in (9) to run from the depth equivalent of ∼20–100 ns) shows this to be true. The range variation of the GPR values becomes much greater [Fig. 6(c), compare light-blue line with dark-blue line]. The greatest difference occurs in the GI and HBI areas where backscatter from within the ice is much less than from the PSS. The change in the SI and firn areas is less significant because the internal scattering sources are of a similar magnitude as the PSS.

Contribution from the PSS to the cross-pol backscatter is of a similar magnitude to sources at greater depth [Fig. 6(b)]. Removing it causes the greatest change in the GI and HBI areas and the least change in the SI and firn areas [Fig. 4(d), compare the dark-blue and light-blue lines]. This is because, as for the co-pols, backscatter from within the GI and HBI is much less than from the PSS. We can estimate the contribution from this layer as ranging from 2 dB in the GI to approximately 0.25 dB in the firn area. This highlights how incoherent scattering at this interface changes upglacier, i.e., greatest in the ice zones and lowest in the firn.

Using both co- and cross-pol responses, the distinct characteristics of the different glacier facies make them fairly easy to delimit on the GPR scattering cross-section profiles (i.e., the two-way time versus distance along the profile images shown in the upper two panels of Figs. 6 and 7). The color-coded bars at the top of Figs. 6 and 7 show how the profiles are interpreted with respect to the glacier facies (note that HBI and GI are a single glacier facies). All profiles in Figs. 3 and 4 have been interpreted in a similar manner. In the next section, this interpretation is superimposed on the SAR images.

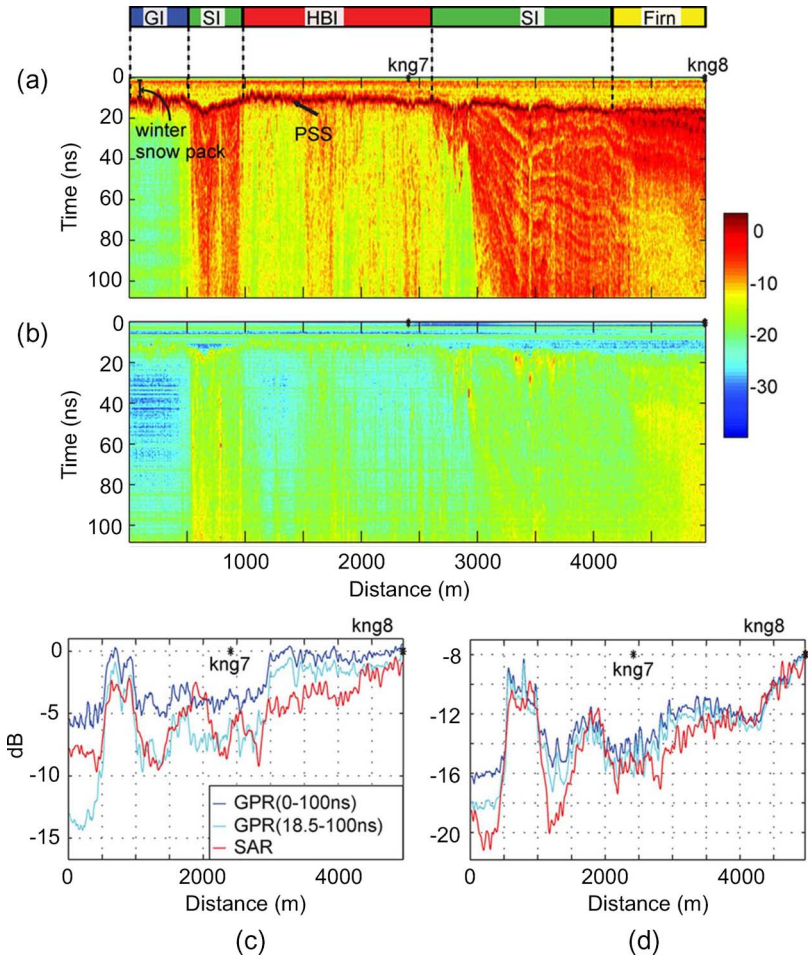

Fig. 7. Profile N2 (location shown in Fig. 1). (a) GPR copolarized radar cross section. (b) GPR cross-polarized radar cross section. The different glacier zones are labeled in the color bar at the top. Blue = glacier ice, red = herringbone ice, green = superimposed ice, and yellow = firn. kng5–kng8 correspond to the stake numbers shown in Fig. 1. The lower panels give the GPR and SAR backscatter coefficient for (c) co-polarized and (d) cross-polarized.

B. SAR Zones

The SAR zones are apparent as different shades in the grayscale SAR image (Fig. 8). By displaying the SAR data in this way (i.e., backscatter coefficient over area), the cross-pol SAR image appears very similar to the co-pol image and, for this reason, is not shown here. The color-coded lines on the image represent the GPR profiles. The colors correspond to the different glacier facies as interpreted from the GPR data (discussed in the previous section). The boundaries between the glacier facies (as seen by the GPR) lie in very close proximity to the SAR zone boundaries, both for co-pol (Fig. 8) and cross-pol. This indicates that the distribution of SAR zones is in agreement with the GPR-derived glacier facies.

Using profiles S1 and N2 as examples, the SAR backscatter coefficient has been extracted along the profiles and compared with the GPR backscatter coefficient [Figs. 6(c) and (d) and 7(c) and (d)]. We see a good resemblance between the values measured by the two systems for the general evolution of the backscatter coefficient upglacier. This fit improves with the removal of the PSS signature from the GPR data. This correction was motivated by the fact that a larger response to this PSS interface is expected for the nadir-looking GPR compared with the side-looking SAR instrument.

For the co-pol response, the PSS-corrected GPR signal (i.e., GPR backscatter coefficient without the PSS signal) has a greater range variation than the SAR backscatter coefficient [Fig. 6(c), compare the red line and the light-blue line]. For the cross-pol response, the increase in the range variation is less and does not exceed that measured by SAR. Noise in the GPR profiles, visible as a horizontal banding, will limit the range variation because it will increase the total backscatter coefficient in areas of low backscatter (i.e., in the GI and HBI areas).

By calculating the system noise from the section of trace before the direct wave, the cross-pol signal-to-noise ratio is above 10 dB for the PSS and between 7 and 13 dB for the SI and firn. The GI area is only noise with the exception of the horizontal banding.

There are some variations within the SAR zones that do not correspond to a change in glacier facies, for example, at the NE end (downglacier end) of profiles N1, S05, and S1 (Fig. 8).

Closer inspection of profile S1 (Fig. 6) shows that, with the PSS removed from the GPR data, an increase and a decrease in the GPR backscatter coefficient occur at the same location as the SAR [Fig. 6(c) and (d), 0–1200 m]. For the GPR, this is due to backscatter sources at depth [seen in Fig. 6(a) and (b)]. These may influence the SAR but is unlikely to cause

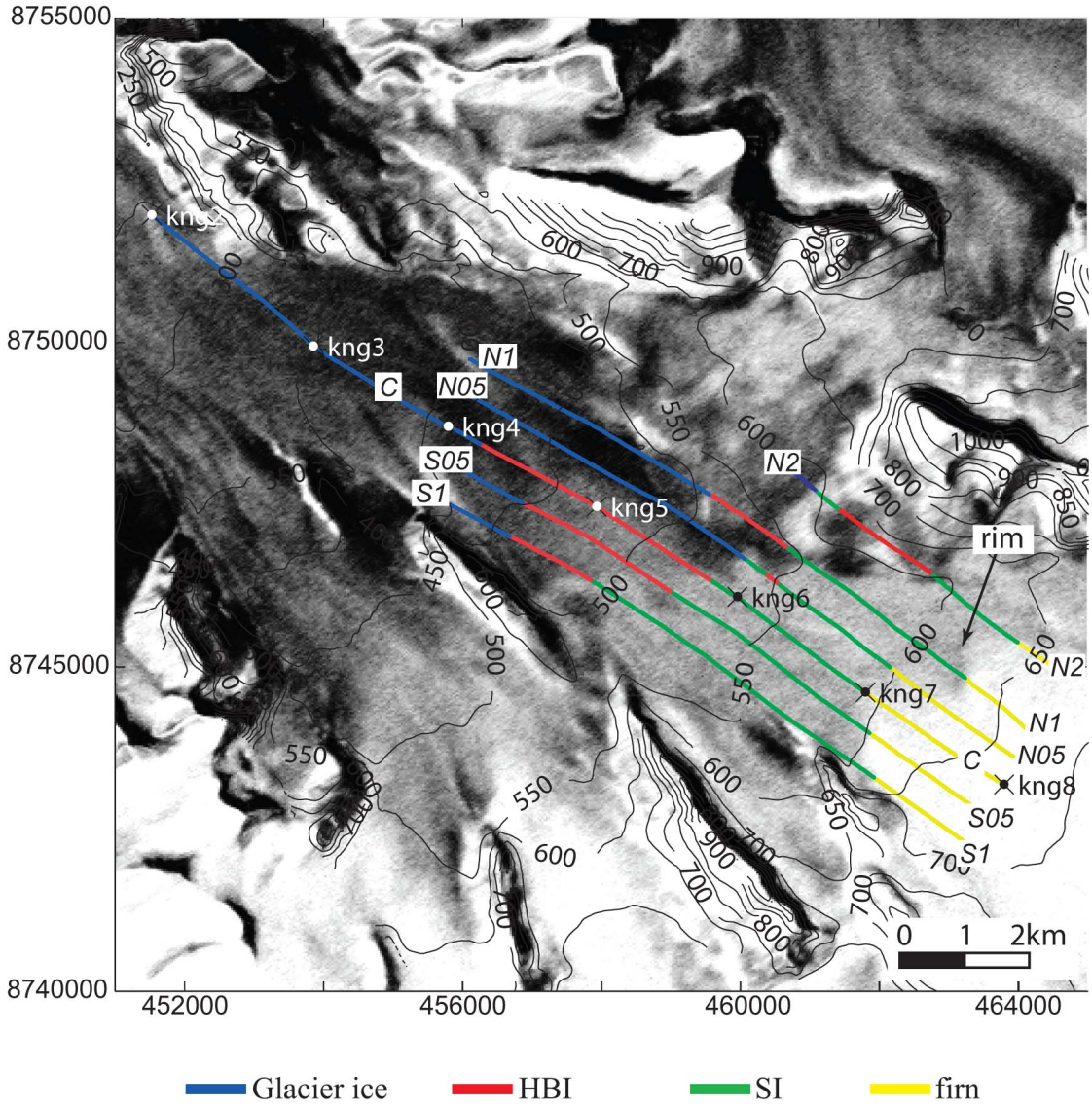

Fig. 8. SAR image (shown on a UTM grid projection) composed of an average of all ascending IS1 and IS2 look-angle copolarized images (HH and VV) listed in Table I. The colored lines indicate the location of the GPR profiles. The profiles are labeled at each end. The interpretation of the different glacier facies using the GPR profiles is indicated by the color coding of the lines. An arrow indicates the dark rim at the onset of the firn area. Profiles S1 (Fig. 6) and N2 (Fig. 7) are discussed in the text.

the 5-dB increase seen in Fig. 6(c) (red line). We suggest instead that the main cause of the high SAR backscatter could be a coherent surface reflection from the PSS interface. This could be from local morphological structures such as drainage channels that create surfaces in the PSS angled favorably for backscatter toward the SAR. We cannot confirm this directly from the PSS morphology seen in the GPR profiles as the SAR look direction is across glacier, perpendicular to the GPR profile direction.

A curious dark rim is visible in the SAR images at the onset of the firn zone (Fig. 8). This rim is due to a drop in the backscatter coefficient [Fig. 9(c) and (d)]. The GPR profiles show that this is the result of an area of relatively low backscatter at depth. There is apparently more structure in this low-backscatter wedge than in pure GI (as seen by the GPR) but less than in the rest of the firn area [Fig. 9(a) and (b)].

VI. Discussion

The different look angles, nadir (0°) for GPR and 15°–27° for SAR, mean that strong nadir reflection components will exist in the GPR data. To account for this, we have applied a 20-dB shift to the GPR backscatter coefficient. This is consistent with experimental results [28] and seems to give a good fit with the SAR backscatter values. This shift does not however compensate for the fact that essentially different viewing geometries may illuminate slightly different volumes [14] and will certainly cause the EM waves to impinge on potential backscatter sources at different angles. It should also be noted that, because we have applied this shift, the backscatter coefficient values cannot be taken as absolute values. Rather, one should focus on the relative changes along the profiles, for which the SAR and GPR can be compared directly. An additional consequence of the different look angles is that the polarization configurations

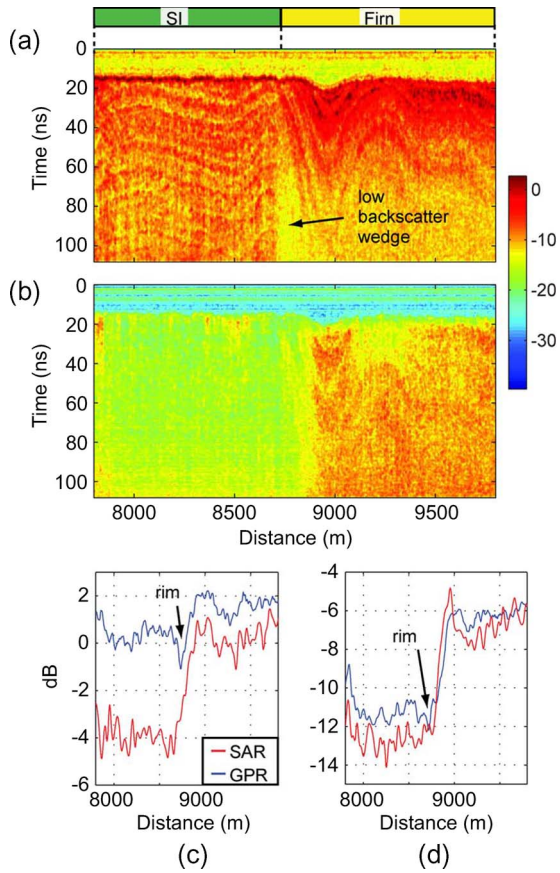

Fig. 9. Illustration of the low-backscatter wedge seen at the SI–firn boundary. (a) GPR copolarized radar cross section. (b) GPR cross-polarized radar cross section. The different glacier zones are labeled in the color bar at the top. Green = superimposed ice and yellow = firn. The lower panels give the GPR and SAR backscatter coefficient for (c) copolarized and (d) cross-polarized.

of the GPR and SAR are not the same. Both X and Y GPR polarizations lie in the SAR H plane. Bearing in mind then that we do not expect the SAR and GPR backscatter coefficients to match exactly at the respective polarizations, the similarities observed here are most encouraging.

The range variation of the GPR co-pol response is increased considerably by removing the contribution from the PSS. This is consistent with limited internal scattering sources in the GI and HBI areas [Fig. 6(a)]. The fact that this causes the GPR range variation to be greater than that measured by SAR indicates that the SAR signature in the low-backscatter GI and HBI regions is also likely to be dominated by scattering at the PSS. Although the SAR response to the PSS is of lower amplitude than the nadir-looking GPR, complete removal of the PSS signature from the GPR results in an underestimation of the SAR response in these areas.

On the other hand, a continued overestimation of the SAR response by the GPR is expected for co-pol in the SI area and, to a lesser extent, in the firn area. This is because interfaces at depth creating coherent reflections that will give higher amplitude returns at the nadir-looking GPR compared with the side-looking SAR. The difference between the SAR and the GPR is likely to be less in the firn area where incoherent scattering is very much more effective.

The similarity between the SAR and the PSS-corrected GPR co-pol response in the SI and firn areas indicates that the SAR signature is also dominated by scattering from below the PSS within these areas.

For the cross-pol response, range variation is limited in the ice facies by noise in the GPR system. Local significant differences between the SAR and GPR backscatter coefficients, which are not explained by suppression of signatures from depth by the PSS [such as 1000–1500 m in Fig. 5(c)] or noise [such as 7000–8000 m in Fig. 4(d)] are attributed to the different viewing geometries of the systems.

The cross-pol GPR profiles show that the roughness of the PSS, as seen by the GPR, varies spatially within the different ice facies. Removal of the PSS from the cross-pol GPR response causes a small vertical shift in the backscatter signature, indicating that all significant zone-defining backscatter signatures originate from below this interface. The co-pol GPR response supports this suggestion, but in this case, the strong return from the PSS, as measured by the GPR, masks the underlying backscatter signature as revealed by SAR. The exception to this is when a favorably oriented PSS interfaces results in a high coherent return to the SAR sensor.

A low-backscatter area at depth at the SI–firn boundary is the cause of the low-backscatter rim around the firn zone (Fig. 8). It is unclear how the composition of this wedge differs from the SI and firn facies or how it forms. It is evidently more homogeneous than firn, rather having a similar scattering potential as SI, but without any layering (Fig. 9). One could imagine that, at this transition between firn and ice, water percolating within the firn and halted at the impermeable SI boundary could freeze at the boundary, causing an ice wedge to accrete. However, we see no clear boundary between this formation and the firn in lower frequency data, as would be expected if this were a wedge of pure ice.

VII. Conclusion

We present 5.3-GHz polarimetric GPR and 5.3-GHz polarimetric satellite SAR profiles from the high-Arctic polythermal glacier Kongsvegen. The data were collected in spring under cold and dry conditions. The GPR data are calibrated and displayed in terms of the equivalent scattering cross section. The backscatter coefficients measured by the two systems are then compared.

Both the co- and cross-pol GPR profiles are used to identify the different glacial facies. It is clear from this exercise that, at these frequencies, the GPR co-pol is best for delimiting the different ice zones, whereas the cross-pol is more useful for locating the SI–firn boundary.

The SAR zones correspond very well with the GPR-defined glacial facies, confirming that 5.3-GHz GPR is a useful tool for further investigation of the SAR signal. We show that the SAR backscatter signal is dominated by significant contributions from subsurface features located below the PSS interface.

Acknowledgment

The Envisat ASAR data used in this paper were provided by the European Space Agency.

REFERENCES

[1] M. König, J. G. Winther, and E. Isaksson, "Measuring snow and glacier ice properties from satellite," *Rev. Geophys.*, vol. 39, no. 1, pp. 1–27, Feb. 2001.

[2] R. Bindschadler, "Monitoring ice sheet behavior from space," *Rev. Geophys.*, vol. 36, no. 1, pp. 79–104, Feb. 1998.

[3] M. Braun, F. Rau, H. Saurer, and H. Gossmann, "Development of radar glacier zones on the King George Island ice cap, Antarctica, during austral summer 1996/97 as observed in ERS-2 SAR data," *Ann. Glaciol.*, vol. 31, no. 1, pp. 357–363, Jan. 2000.

[4] L. C. Smith, R. R. Forster, B. L. Isacks, and D. K. Hall, "Seasonal climatic forcing of alpine glaciers revealed with orbital synthetic aperture radar," *J. Glaciol.*, vol. 43, no. 145, pp. 480–488, 1997.

[5] R. R. Forster, B. L. Isacks, and S. B. Das, "Shuttle imaging radar (SIR-C/X-SAR) reveals near-surface properties of the South Patagonian icefield," *J. Geophys. Res.—Planets*, vol. 101, no. E10, pp. 23 169–23 180, 1996.

[6] G. J. Marshall, W. G. Rees, and J. A. Dowdewell, "The discrimination of glacier facies using multitemporal ERS-1 SAR data," in *Proc. 14th EARSeL Symp.—Sensors and Environmental Applications of Remote Sensing*, Göteborg, Sweden, 1994, pp. 263–269.

[7] K. C. Partington, "Discrimination of glacier facies using multi-temporal SAR data," *J. Glaciol.*, vol. 44, no. 146, pp. 42–53, 1998.

[8] W. H. Stiles and F. T. Ulaby, "The active and passive microwave response to snow parameters. 1. Wetness," *J. Geophys. Res.*, vol. 85, no. C2, pp. 1037–1044, Feb. 1980.

[9] C. Mätzler, "Applications of the interaction of microwaves with the natural snow cover," *Remote Sens. Rev.*, vol. 2, no. 2, pp. 259–387, 1987.

[10] E. Rignot, "Backscatter model for the unusual radar properties of the Greenland ice sheet," *J. Geophys. Res.—Planets*, vol. 100, no. E5, pp. 9389–9400, May 25, 1995.

[11] K. C. Jezek, P. Gogineni, and M. Shanableh, "Radar measurements of melt zones on the Greenland ice sheet," *Geophys. Res. Lett.*, vol. 21, no. 1, pp. 33–36, Jan. 1, 1994.

[12] M. König, J. Wadham, J. G. Winther, J. Kohler, and A. M. Nuttall, "Detection of superimposed ice on the glaciers Kongsvegen and Midre Lovenbreen, Svalbard, using SAR satellite imagery," *Ann. Glaciol.*, vol. 34, no. 1, pp. 335–342, Jan. 2002.

[13] J. B. T. Scott, D. Mair, P. Nienow, V. Parry, and E. Morris, "A ground-based radar backscatter investigation in the percolation zone of the Greenland ice sheet," *Remote Sens. Environ.*, vol. 104, no. 4, pp. 361–373, Oct. 2006.

[14] K. Langley, S.-E. Hamran, K. A. Høgda, R. Storvold, O. Brandt, J. O. Hagen, and J. Kohler, "Use of C-band ground penetrating radar to determine backscatter sources within glaciers," *IEEE Trans. Geosci. Remote Sens.*, vol. 45, no. 5, pp. 1236–1246, May 2007.

[15] J. Wadham, J. Kohler, A. Hubbard, A. M. Nuttall, and D. Rippin, "Superimposed ice regime of a high Arctic glacier inferred using ground-penetrating radar, flow modeling, and ice cores," *J. Geophys. Res.—Earth Surface*, vol. 111, no. F1, F01007, Feb. 2006.

[16] S.-E. Hamran, E. Aarholt, J. O. Hagen, and P. Mo, "Estimation of relative water content in a sub-polar glacier using surface-penetration radar," *J. Glaciol.*, vol. 42, no. 142, pp. 533–537, 1996.

[17] S.-E. Hamran, T. Guneriussen, J. O. Hagen, and R. Odegard, "Ground penetration radar and ERS SAR data for glacier monitoring," in *Proc. IGARSS*, 1997, pp. 634–636.

[18] H. Björnsson, Y. Gjessing, S. E. Hamran, J. O. Hagen, O. Liestol, F. Palsson, and B. Erlingsson, "The thermal regime of sub-polar glaciers mapped by multi-frequency radio-echo sounding," *J. Glaciol.*, vol. 42, no. 140, pp. 23–32, 1996.

[19] G. D. Q. Robin, S. Evans, and J. T. Bailey, "Interpretation of radio echo sounding in polar ice sheets," *Philos. Trans. R. Soc. Lond. Ser. A: Math. Phys. Sci.*, vol. 265, no. 1166, pp. 437–505, Dec. 1969.

[20] O. Liestøl, "The glaciers in the Kongsfjorden area, Spitsbergen," *Det Norske Geografiske Tidsskrift*, vol. 42, pp. 231–238, 1988.

[21] J. O. Hagen, K. Melvold, F. Pinglot, and J. A. Dowdeswell, "On the net mass balance of the glaciers and ice caps in Svalbard, Norwegian Arctic," *Arctic Antarctic Alpine Res.*, vol. 35, no. 2, pp. 264–270, May 2003.

[22] L. A. Rasmussen and J. Kohler, "Mass balance of three Svalbard glaciers reconstructed back to 1948," *Polar Res.*, vol. 26, no. 2, pp. 168–174, Sep. 2007.

[23] O. Brandt, J. Kohler, and M. Luthje, "Spatial mapping of multi-year superimposed ice on the glacier Kongsvegen, Svalbard," *J. Glaciol.*, vol. 54, no. 184, pp. 73–80, 2008.

[24] S.-E. Hamran and K. Langley, "C-band polarimetric GPR," in *Proc. 11th Int. Conf. Ground Penetrating Radar*, Columbus, OH, 2006.

[25] D. J. Daniels, *Ground Penetrating Radar*, 2nd ed. London, U.K.: IEE, 2004.

[26] K. Sarabandi, F. T. Ulaby, and M. A. Tassoudji, "Calibration of polarimetric radar systems with good polarization isolation," *IEEE Trans. Geosci. Remote Sens.*, vol. 28, no. 1, pp. 70–75, Jan. 1990.

[27] K. Langley, P. Lacroix, S.-E. Hamran, and O. Brandt, "Sources of backscatter at 5.3 GHz from the superimposed ice and firn area revealed by multi-frequency GPR and cores," *J. Glaciol.*, 2007. to be published.

[28] C. Mätzler, T. Strozzi, T. Weise, D. M. Floricioiu, and H. Rott, "Microwave snowpack studies made in the Austrian Alps during the SIR-C/X-SAR experiment," *Int. J. Remote Sens.*, vol. 18, no. 12, pp. 2505–2530, Aug. 1997.

[29] H. Johnsen, I. Lauknes, and T. Guneriussen, "Geocoding of fast-delivery SAR image mode product using DEM data," *Int. J. Remote Sens.*, vol. 16, no. 11, pp. 1957–1968, 1995.

[30] I. Lauknes and E. Malnes, "Automatical geocoding of SAR products," in *Proc. Envisat ERS Symp.*, Salzburg, Austria, 2004.

[31] F. Obleitner and M. Lehning, "Measurement and simulation of snow and superimposed ice at the Kongsvegen glacier, Svalbard (Spitzbergen)," *J. Geophys. Res.—Atmos.*, vol. 109, no. D4, pp. D04106.1–D04106.12, Feb. 25, 2004.

[32] J. L. Wadham and A. M. Nuttall, "Multiphase formation of superimposed ice during a mass-balance year at a maritime high-Arctic glacier," *J. Glaciol.*, vol. 48, no. 163, pp. 545–551, Dec. 2002.

Kirsty Langley was born in England, U.K., in 1977. She received the M.Sc. degree in geophysics from the University of Iceland, Reykjavik, Iceland, in 2000, and the Ph.D. degree from the Department of Geoscience, University of Oslo, Oslo, Norway, in 2007.

She is currently a Postdoc with the Norwegian Polar Institute, Tromsø, Norway, and the Institute of Physics and Technology, University of Tromsø, Tromsø. Her research focus is on ground-penetrating radar and remote sensing investigations of glaciers.

Svein-Erik Hamran received the M.Sc. degree in technical physics from the Norwegian Institute of Technology, Trondheim, in 1984, and the Dr.Sci. (Ph.D.) degree in applied physics from the University of Tromsø, Tromsø, Norway, in 1990.

From 1985 to 1996, he was with the Environmental Surveillance Technology Programme, and from 1989 to 1990, he was a Visiting Scientist with the CNRS Service d'Aeronomie, where he worked on the Mars 96 GPR radar PRISM. Since 1996, he has been with the Norwegian Defence Research Establishment, Kjeller, Norway, as a Chief Scientist managing the radar programs. Since 2001, he has been an Adjunct Professor in environmental geophysics with the University of Oslo, Oslo, Norway. He is a Coinvestigator on the ESA satellite ROSETTA experiment Comet Nucleus Sounding Experiment by Radiowave Transmission (CONSERT) and a Deputy Team Leader on the WISDOM GPR experiment on the ESA ExoMars satellite. His main research interests includes radar imaging and ground-penetrating radar design and modeling.

Kjell Arild Høgda received the M.Sc. and Ph.D. degrees in applied physics (remote sensing) from the University of Tromsø, Tromsø, Norway, in 1988 and 1994, respectively.

From 1988 to 2003, he was a Research Scientist with the NORUT Information Technology (IT), Tromsø. Since 2003, he has been the Research Manager of the Earth Observation Group, NORUT IT. He has worked on a broad spectrum of satellite remote sensing applications, including ocean color measurements, snow and ice monitoring, vegetation classification, pollution impact studies, SAR interferometry, SAR ocean wave imaging, and phenology for climate-change impact studies. Currently, he is the Project Leader of the Norwegian Research Council-funded EnviTools project, where the goal is to enhance the understanding of the interaction of microwaves with snow and glacier ice.

Rune Storvold (M'04) received the B.S. and M.S. degrees from the University of Bergen, Bergen, Norway, and the Ph.D. degree from the University of Alaska Fairbanks, Fairbanks, Alaska, in 2001.

From 2001 to 2003, he was a Research Professional with the Geophysical Institute, University of Alaska Fairbanks. He is currently a Senior Scientist with the NORUT Information Technology, Tromsø, Norway. His research interests include remote sensing of ocean, snow, ice, and atmospheric properties, as well as radiative transfer modeling. Currently, he is also working on establishing an airborne unmanned measurement platform to supplement and validate satellite data within these fields.

Ola Brandt received the M.S. degree from the University of Bergen, Bergen, Norway, and the Ph.D. degree in geosciences from the University of Oslo, Oslo, Norway, in 2007.

He is currently with the Norwegian Polar Institute, Tromsø, and is involved in the validation of radar altimeter data from ice sheets, as well as ground-based radar studies of glaciers including coring and numerical electromagnetic modeling.

Jack Kohler received the B.A. degree from the University of Pennsylvania, Philadelphia, in 1983, and the Ph.D. degree from the University of Minnesota, Minneapolis, in 1992.

He is a Glaciologist with the Norwegian Polar Institute, Tromsø, Norway. He has over 20 years of experience in arctic fieldwork and in two field seasons in Antarctica. His current research interests include the relation between climate and glacier mass balance, the use of GPR in operational glaciology, the relation between ice-core dielectric properties and GPR imagery, and the relation of snowpack dynamics to terrestrial ecosystems.

Jon Ove Hagen was born in Ringebu, Norway, in 1950. He received the Cand.Real. (M.Sc.) degree in mathematics, physics, and geography/glaciology and the Dr.Sci. (Ph.D.) degree in glaciology from the University of Oslo, Oslo, Norway, in 1978 and 1986, respectively.

From 1986 to 1993, he was a Glaciologist with the Norwegian Polar Institute (NPI), Tromsø, where he was responsible for NPI's glaciological investigations in Svalbard. From 1993 to 1995, he was the Head of the Snow and Glacier Section, Hydrology Department, Norwegian Water Resources and Energy Administration, where he was responsible for glacier monitoring in Norway. Since 1994, he has been with the Department of Geosciences, University of Oslo. Since 1996, he has been a Professor with the Department of Geography, University of Oslo, where, from 1997 to 2003, he was the Head of the department. He has over 20 years of experience in the field of glaciology, with a focus on mass balance studies.

Dr. Hagen has been a member of the International Glaciological Society (IGS) since 1980 and was a council member of IGS from 2002 to 2006. He was the Chairman of the International Arctic Science Committee Working Group on Arctic Glaciology from 1995 to 2003 and the Vice President of the International Commission of Snow and Ice from 1999 to 2006.